Onset of convection in two liquid layers with phase change

G. B. McFadden,[a] S. R. Coriell, K. F. Gurski,[b] and D. L. Cotrell[c]
National Institute of Standards and Technology, Gaithersburg, Maryland 20899, USA

(Received 18 May 2007; accepted 26 September 2007; published online 31 October 2007)

We perform linear stability calculations for horizontal fluid bilayers that can undergo a phase transformation, taking into account both buoyancy effects and thermocapillary effects in the presence of a vertical temperature gradient. We find that the entropy difference between the phases plays a crucial role in determining the stability of the system. For small values of the entropy difference between the phases, the system can be linearly unstable to heating from either above or below. The instability is due to the Marangoni effect in combination with the effects of buoyancy (for heating from below). For larger values of the entropy difference, the system is unstable only to heating from below, and the driving force for the instability is thermodynamic in nature, dominating the Marangoni effect. This long-wavelength instability can be understood qualitatively in terms of a variation of the classical morphological stability analysis of a phase boundary. The interface is unstable if either of the adjacent bulk phases is thermodynamically unstable. To help elucidate the mechanisms driving the instability on heating from below, we have performed both long-wavelength and short-wavelength analyses of the two-phase system, and have performed numerical calculations using materials parameters for a water-steam system. The two-phase system also allows a conventional Rayleigh-Taylor instability if the heavier fluid overlies the lighter fluid; applying a temperature gradient allows a stabilization of the interface. © *2007 American Institute of Physics*. [DOI: 10.1063/1.2800339]

I. INTRODUCTION

The study of the stability of a fluid-fluid interface is important in a number of scientific and technological applications. In this paper we consider two fluid layers separated by a horizontal planar interface subject to a vertical temperature gradient. The case of two fluids that are, to a greater or lesser degree, immiscible, has been well studied both theoretically and experimentally,[1–8] and the effects of various driving forces on the stability of the system have been taken into account. Examples include the effects of buoyancy (natural or Rayleigh-Bénard convection[9]), the effects of bulk density differences (Rayleigh-Taylor instabilities[10–14]), and the effects of surface tension gradients along the interface (Marangoni instabilities[3]).

This situation can be contrasted with that of a bilayer system in which the two layers represent different phases of a single fluid.[15–22] The phase transformation that may then occur between the two layers is described by a modification of the usual interfacial boundary conditions that are used to describe immiscible fluids. For a two-phase system there can be mass flow across the interface, which is not a material surface. In addition, latent heat is typically generated at the interface which is conducted into the surrounding fluid. Finally, a description of the thermodynamic state of the interface is required, which is often based either on an assumption of local thermodynamic equilibrium or a kinetic statement governing systematic deviations from local thermodynamic equilibrium. As a result, the stability results for a two-phase bilayer system are quantitatively and even qualitatively different than those for an immiscible system. Examples of the two-phase case arise in many material processing applications.

Many studies of bilayer instabilities of an immiscible system consider two fluids with materials properties that are sufficiently different in the two phases that one of the layers is passive, and can be neglected to produce a simpler single-layer system. In addition, if the effects of surface tension are strong enough, the deflection of the interface may be neglected, resulting in further simplification of the analysis. In contrast, two-phase systems often arise near the thermodynamic critical point of a single-component fluid or in cases of phase separation in multicomponent systems. In these systems, the material constants in each phase are often of similar magnitude, particularly close to the transition points where the two phases become indistinguishable. Examples of single-component systems include the water-steam system as used in the power industry, and examples of phase-separating multicomponent systems include the cases of spinodal decomposition and of monotectic growth.

In this paper we consider a simplified bilayer geometry in which a horizontal interface separates two semi-infinite layers of a single-component fluid. This problem is still sufficiently complex that we generally resort to a numerical determination of the linear stability of the system, including the possibility of oscillatory modes and significant interfacial deformations. The governing equations contain a large number of dimensionless parameters, including a Rayleigh number,

[a]Author to whom correspondence should be addressed. Telephone: +1-301-975-2711. Fax +1-301-975-3553. Electronic mail: mcfadden@nist.gov
[b]Current address: Department of Mathematics, George Washington University, Washington, DC 20052., USA.
[c]Current address: Lawrence Livermore National Laboratory, Livermore, CA 94550, USA.

Marangoni number, Bond number, Crispation number, and ratios of material properties of the two phases. We consider material parameters appropriate for a water-steam system. We find particularly interesting stability results at low wavenumbers, for a mode that is sensitive to the differences in enthalpy and entropy between the two phases. To examine this mode in more detail, we perform a small-wavenumber expansion of the stability problem, finding that the mode is also sensitive to the values of both the Bond and Crispation numbers of the system.

For simplicity, we assume that local equilibrium holds at the fluid-fluid interface. More general boundary conditions that apply under nonequilibrium conditions have been discussed by a number of authors.[18,20–22] These conditions can also be derived by considering sharp-interface limits[23] of diffuse interface models.[24–26] We note that the assumption of local equilibrium at the phase boundary does not preclude evaporation or condensation that accompanies interface motion; however, in our case we consider a static base state that supports a heat flux through the system without phase change, so that evaporation or condensation are small effects associated with the perturbed system.

We find that a two-phase system that is heated from below is subject to a type of morphological instability at small wavenumbers that is similar in origin to other, more familiar, instabilities that occur in materials processing applications.[27] Multiphase systems are typically subject to instability if one or more of the phases is in a thermodynamic state of metastability; specifically, if there are regions of space where the actual phase of the system is not the phase of lowest free energy under the given conditions.[28–31] The driving force for an instability is the release of free energy accompanying a phase transformation from the higher energy phase to the lower energy phase. In practice, the nucleation of the lower energy phase in the bulk unstable phase is rarely observed under conditions of mild disequilibrium, since there is an accompanying energy penalty associated with the creation of surface area of the new phase. However, the energy difference can drive the instability at an interface where the two phases come in contact. The resulting instability generally displays a wavelength that is determined by a balance between surface energy (stabilizing) and the difference in bulk free energy between the phases (destabilizing).

A portion of the phase diagram for a representative water-steam system is depicted in Fig. 1. A two-phase system consisting of liquid and gas is in thermodynamic equilibrium along the coexistence curve in pressure-temperature space. The coexistence curve terminates at the thermodynamic critical point where the properties of the liquid and gas become equal. The liquid phase is preferred under conditions of higher pressure and lower temperature, and the gas phase is preferred for lower pressures and higher temperatures. The slope of the coexistence curve is given by the Clausius-Clapeyron equation[32]

$$\frac{dp}{dT} = \frac{(s_m^\alpha - s_m^\beta)}{(1/\bar{\rho}_\alpha - 1/\bar{\rho}_\beta)}, \tag{1}$$

where s_m^α and s_m^β are the entropy densities of the phases, and $\bar{\rho}_\alpha$ and $\bar{\rho}_\beta$ are the densities; here we assume the lighter gas phase (α) overlies the denser liquid phase (β). If the bilayer is heated from below, the respective static pressure and temperature profiles $p(z)$ and $T(z)$ in each phase satisfy $dp=-\rho g dz$ and $dT=Gdz$, where z is the vertical coordinate, g is the gravitational acceleration, and G denotes the temperature gradient, which is negative for heating from below. The condition that the liquid is superheated or that the gas is supercooled relative to thermodynamic equilibrium can be determined graphically by plotting the respective pressure and temperature profiles $p(z)$ and $T(z)$ in relation to the coexistence curve, or by comparing the slopes $dp/dT=-\rho g/G$ at the interface in each phase with that given by the Clausius-Clapeyron equation. This relation gives the correct qualitative form for the observed long-wavelength instability, but it is not quantitatively accurate since the instability involves lateral pressure and temperature gradients along the interface that drive convection and alter the thermal transport in the system. Our results include the derivation of a quantitative version of this expression that is obtained by performing a small-wavenumber expansion for the full governing equations, including the effects of convection. The predictions are in good agreement with the corresponding numerical results that we obtain.

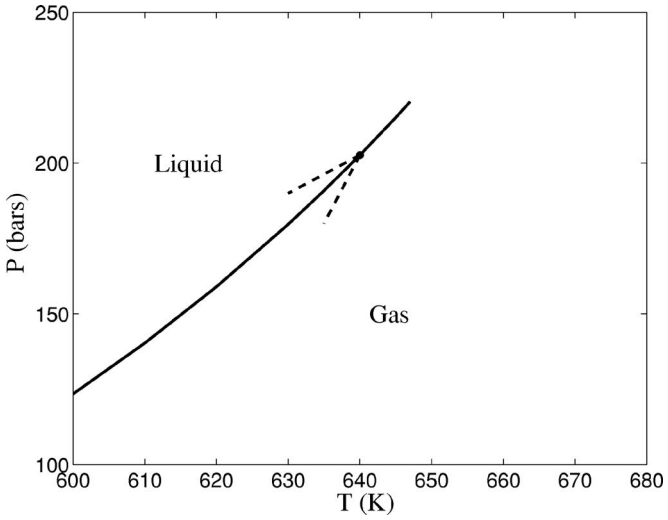

FIG. 1. Phase diagram for the water-steam system near its critical point. The solid curve is the coexistence curve for the two-phase system, representing the locus of equilibrium temperatures and pressures and terminating at the critical point where the properties of the liquid and gas phases become identical. The two dashed curves represent schematic profiles of $T(z)$ and $p(z)$, respectively, in the gas layer. If the dashed curve has a small enough slope, it lies within the liquid region of the phase diagram and represents a supercooled gas state. A similar diagram applies for the profile in the liquid layer, where a superheated liquid state is possible if the corresponding slope is sufficiently small.

The paper is organized as follows. Governing equations are given in the next section. The numerical procedure is described briefly in Sec. III. Linear stability results are presented next, including a comparison of the numerical results with large- and small-wavenumber expansions. A discussion is presented in Sec. V, followed by conclusions in Sec. VI. The Appendix contains a summary of the expansion results.

II. EQUATIONS

We consider a semi-infinite horizontal two-layer system, with vertical heating across the layers. The unperturbed upper layer (denoted by α) extends over the interval $0<z<H_\alpha$, and the unperturbed lower layer (denoted by β) extends over the interval $-H_\beta<z<0$. Without loss of generality, we consider linear stability results for a two-dimensional system. The horizontal coordinate extends over the interval $-\infty<x<\infty$, and the velocity $\mathbf{u}$ has components in the x and z directions given by u and w, respectively.

A. Governing equations in the bulk

In each phase α and β, we consider the Boussinesq equations

$$\boldsymbol{\nabla}\cdot\mathbf{u}=0, \tag{2}$$

$$\bar{\rho}\mathbf{u}_t+\bar{\rho}(\mathbf{u}\cdot\boldsymbol{\nabla})\mathbf{u}+\boldsymbol{\nabla}p=\mu\nabla^2\mathbf{u}-\rho g\mathbf{z}, \tag{3}$$

$$T_t+(\mathbf{u}\cdot\boldsymbol{\nabla})T=\kappa\nabla^2T. \tag{4}$$

Here, p is the pressure, μ is the dynamic viscosity, T is the temperature, κ is the thermal diffusivity, g is the gravitational acceleration, t is the time, and $\mathbf{z}$ is the unit vector in the z direction (anti-parallel to gravity). With the exception of the density, we assume the material properties are constant in each phase, although the properties can differ from phase to phase, and will be distinguished by subscripts α and β. We assume the density ρ in each phase is constant in all terms except the gravitational terms, where the densities are given by

$$\rho_\alpha=\bar{\rho}_\alpha(1-\eta_\alpha[T-T_R]),\quad \rho_\beta=\bar{\rho}_\beta(1-\eta_\beta[T-T_R]). \tag{5}$$

Here, $\bar{\rho}_\alpha$ and $\bar{\rho}_\beta$ are the densities in each phase at the reference temperature T_R, and the thermal expansion coefficients η_α and η_β are assumed to be constant in each phase.

B. Boundary conditions

The upper boundary at $z=H_\alpha$ and the lower boundary at $z=-H_\beta$ are assumed to be isothermal with no-slip boundary conditions. The interface is assumed to have the form $z=h(x,t)$.

The temperature is continuous across the interface,

$$[\![T]\!]=0, \tag{6}$$

where $[\![T]\!]=T^\alpha-T^\beta$ denotes the temperature jump across the interface. The tangential velocity is assumed to satisfy the no-slip condition

$$[\![\mathbf{u}\cdot\mathbf{t}]\!]=0, \tag{7}$$

where $\mathbf{t}$ is any tangent vector to the interface. The stress boundary condition is

$$[\![\bar{\rho}\mathbf{u}(\mathbf{u}\cdot\mathbf{n}-v_n)]\!]=[\![\mathbb{T}\cdot\mathbf{n}]\!]-\gamma\mathcal{K}\mathbf{n}+\boldsymbol{\nabla}_S\gamma, \tag{8}$$

where $\mathbf{n}$ is a unit normal vector to the interface, $\mathbb{T}_{jk}=-p\delta_{jk}+\mu(\partial u_j/\partial x_k+\partial u_k/\partial x_j)$ is the stress tensor, γ is the surface tension, $\mathcal{K}$ is the curvature, v_n is the normal velocity of the interface, and $\boldsymbol{\nabla}_S$ is the surface gradient. Here, our sign convention is that the curvature $\mathcal{K}$ is defined to be positive for a spherical inclusion of β phase. For example, in two dimensions with an interface $y=h(x,t)$, the curvature is $\mathcal{K}=-h_{xx}/[1+h_x^2]^{3/2}$, the interface velocity is $v_n=h_t/[1+h_x^2]^{1/2}$, and the surface gradient of the temperature-dependent surface energy $\gamma=\gamma(T)$ is given by

$$\boldsymbol{\nabla}_S\gamma=\gamma_T\frac{(T_x+h_xT_y)}{\sqrt{1+h_x^2}}\mathbf{t}, \tag{9}$$

where $\gamma_T=d\gamma/dT$ and $\mathbf{t}$ is the unit tangent vector to the interface in the direction of increasing x. Here, h_{xx} indicates the second derivative of h, etc.

Mass conservation across the interface takes the form

$$[\![\bar{\rho}(\mathbf{u}\cdot\mathbf{n}-v_n)]\!]=0. \tag{10}$$

Thermodynamic equilibrium at the interface is given by

$$[\![g_m(T,p)]\!]=0, \tag{11}$$

where $g_m(T,p)$ is the Gibbs free energy density, with $dg_m=-s_mdT+dp/\rho$, and s_m is the entropy density. The balance of energy at the interface can be expressed in the form

$$\left[\!\!\left[\rho\left(e_m+\frac{1}{2}|\mathbf{u}|^2\right)(\mathbf{u}\cdot\mathbf{n}-v_n)\right]\!\!\right]=[\![\mathbb{T}\mathbf{u}]\!]\cdot\mathbf{n}-\left[\!\!\left[k\frac{\partial T}{\partial n}\right]\!\!\right], \tag{12}$$

where e_m is the internal energy density and k is the thermal conductivity. Using Eq. (10), this can be written in the form of a flux balance

$$\left[\!\!\left[k\frac{\partial T}{\partial n}\right]\!\!\right]=\bar{\rho}_\alpha(\mathbf{u}^\alpha\cdot\mathbf{n}-v_n)L_{\alpha\beta}, \tag{13}$$

where $L_{\alpha\beta}=h_m^\alpha-h_m^\beta$ is the difference in enthalpy density $h_m=e_m+p/\rho$ between the phases; for simplicity, we have also neglected some nonlinear convective terms that have no effect on linear stability.

C. Base state

We linearize about a quiescent base state (also indicated by bars). The thermal field is

$$\bar{T}^\alpha(z)=T_E+G_\alpha z \tag{14}$$

in the α phase, and

$$\bar{T}^\beta(z)=T_E+G_\beta z \tag{15}$$

in the β phase, where T_E is the unperturbed interface temperature. The temperature gradients in the base state satisfy

$$0=k_\alpha G_\alpha-k_\beta G_\beta. \tag{16}$$

The pressure field in the base state is hydrostatic, with

$$\frac{d\bar{p}^\alpha}{dz}=-\bar{\rho}_\alpha g,\quad \frac{d\bar{p}^\beta}{dz}=-\bar{\rho}_\beta g. \tag{17}$$

Note that we assume that the base state consists of a static planar interface. Although there is a heat flux through the system that can drive instabilities, in the base state there is no transformation of phase taking place (i.e., no evaporation of liquid or condensation of vapor).

TABLE I. Thermophysical properties of the steam (α phase) water (β phase) system at the equilibrium state with T_E=640 K and p_E=202.7 bar used in the numerical calculations.

Property	Symbol	Value	Unit
Density of water	ρ_β	481.6	kg/m^3
Density of steam	ρ_α	177.4	kg/m^3
Dynamic viscosity of water	μ_β	5.526×10^{-5}	Pa s
Dynamic viscosity of steam	μ_α	2.795×10^{-5}	Pa s
Thermal conductivity of water	k_β	0.4177	W/mK
Thermal conductivity of steam	k_α	0.2499	W/mK
Thermal diffusivity of water	κ_β	$3.276(10^{-8})$	m^2/s
Thermal diffusivity of steam	κ_α	2.682×10^{-8}	m^2/s
Surface energy	γ	8.09×10^{-4}	J/ m^2
$d\gamma/dT$	γ_T	-1.42×10^{-4}	J/K m^2
Thermal expansion coefficient of water	η_β	3.94×10^{-2}	K^{-1}
Thermal expansion coefficient of steam	η_α	7.34×10^{-2}	K^{-1}
Difference in entropy density	$s_{\alpha\beta}=s_m^\alpha-s_m^\beta$	8.632×10^2	J/K kg
Difference in enthalpy density (latent heat)	$L_{\alpha\beta}=T_E s_{\alpha\beta}=h_m^\alpha-h_m^\beta$	5.524×10^5	J/kg
Total thickness of layer	d	2.0×10^{-3}	m
Gravitational acceleration	g	9.8	m/s^2

D. Dimensionless parameters and linearized governing equations

Following the treatment in Ref. 1, we make the equations dimensionless based on a length scale given by the total depth $d=H_\alpha+H_\beta$, a time scale based on the thermal time d^2/κ_β, a velocity scale κ_β/d, a temperature scale $G_\beta d$, and a pressure scale $\nu_\beta\kappa_\beta\bar{\rho}_\beta/d^2$. These scales introduce the dimensionless parameters

$$\nu^*=\frac{\nu_\alpha}{\nu_\beta},\quad \rho^*=\frac{\bar{\rho}_\alpha}{\bar{\rho}_\beta},\quad \eta^*=\frac{\eta_\alpha}{\eta_\beta}, \tag{18}$$

$$\kappa^*=\frac{\kappa_\alpha}{\kappa_\beta},\quad k^*=\frac{k_\alpha}{k_\beta},\quad G^*=\frac{G_\alpha}{G_\beta},\quad \mu^*=\frac{\mu_\alpha}{\mu_\beta}, \tag{19}$$

$$\mathrm{Pr}=\frac{\nu_\beta}{\kappa_\beta},\quad \mathrm{Ra}=\frac{g\eta_\beta G_\beta d^4}{\nu_\beta\kappa_\beta},\quad \mathrm{Cr}=\frac{\mu_\beta\kappa_\beta}{d\gamma},$$
$$\mathrm{Bo}=\frac{g\rho_\beta d^2}{\gamma},\quad \mathrm{Ma}=-\frac{\gamma_T G_\beta d^2}{\mu_\beta\kappa_\beta}, \tag{20}$$

$$\mathcal{L}_{\alpha\beta}=\frac{\rho_\beta L_{\alpha\beta}\kappa_\beta}{k_\beta G_\beta d},\quad \mathcal{S}_{\alpha\beta}=\frac{s_{\alpha\beta}G_\beta d^3}{\nu_\beta\kappa_\beta},\quad \ell=\frac{-H_\beta}{H_\alpha}. \tag{21}$$

Here, ℓ is a geometrical parameter, and $s_{\alpha\beta}=s_m^\alpha-s_m^\beta$ is the difference in entropy density between the phases, so that $\mathcal{L}_{\alpha\beta}$ and $\mathcal{S}_{\alpha\beta}$ represent a dimensionless latent heat and dimensionless entropy difference, respectively (see Table I). We note that in dimensional terms, these quantities are related by $L_{\alpha\beta}=T_E s_{\alpha\beta}$, where T_E is the equilibrium transition temperature at the interface. Since the proportionality factor T_E does not appear in any other parameters, $\mathcal{L}_{\alpha\beta}$ and $\mathcal{S}_{\alpha\beta}$ represent independent dimensionless parameters. We note that $\mu^*=\rho^*\nu^*$ and $k^*G^*=1$.

We assume a horizontal wavenumber a and a temporal growth rate $\sigma=\sigma_r+i\sigma_i$. The perturbed quantities (indicated by tildes) then satisfy

$$ia\tilde{u}^\alpha+\tilde{w}_z^\alpha=0, \tag{22}$$

$$\mathrm{Pr}^{-1}\sigma\tilde{u}^\alpha+ia\tilde{p}^\alpha/\rho^*=\nu^*(\tilde{u}_{zz}^\alpha-a^2\tilde{u}^\alpha), \tag{23}$$

$$\mathrm{Pr}^{-1}\sigma\tilde{w}^\alpha+\tilde{p}_z^\alpha/\rho^*=\nu^*(\tilde{w}_{zz}^\alpha-a^2\tilde{w}^\alpha)+\eta^*\mathrm{Ra}\tilde{T}^\alpha, \tag{24}$$

$$\sigma\tilde{T}^\alpha+G^*\tilde{w}^\alpha=\kappa^*(\tilde{T}_{zz}^\alpha-a^2\tilde{T}^\alpha), \tag{25}$$

for $z>0$, and

$$ia\tilde{u}^\beta+\tilde{w}_z^\beta=0, \tag{26}$$

$$\mathrm{Pr}^{-1}\sigma\tilde{u}^\beta+ia\tilde{p}^\beta=\tilde{u}_{zz}^\beta-a^2\tilde{u}^\beta, \tag{27}$$

$$\mathrm{Pr}^{-1}\sigma\tilde{w}^\beta+\tilde{p}_z^\beta=\tilde{w}_{zz}^\beta-a^2\tilde{w}^\beta+\mathrm{Ra}\tilde{T}^\beta, \tag{28}$$

$$\sigma\tilde{T}^\beta+\tilde{w}^\beta=\tilde{T}_{zz}^\beta-a^2\tilde{T}^\beta, \tag{29}$$

for $z<0$. Henceforth, all variables are considered to be dimensionless.

The boundary conditions at $z=0$ are

$$\tilde{T}^\alpha+G^*\tilde{h}=\tilde{T}^\beta+\tilde{h}, \tag{30}$$

$$\tilde{u}^\alpha-\tilde{u}^\beta=0, \tag{31}$$

$$(\tilde{p}^\alpha-\tilde{p}^\beta)-\mathrm{Bo}\,\mathrm{Cr}^{-1}(\rho^*-1)\tilde{h}+a^2\mathrm{Cr}^{-1}\tilde{h}=2(\mu^*\tilde{w}_z^\alpha-\tilde{w}_z^\beta), \tag{32}$$

$$(\mu^*\tilde{u}_z^\alpha-\tilde{u}_z^\beta)+ia(\mu^*\tilde{w}^\alpha-\tilde{w}^\beta)-ia\,\mathrm{Ma}(\tilde{T}^\alpha+G^*\tilde{h})=0, \tag{33}$$

$$\mathcal{S}_{\alpha\beta}[\tilde{T}^{\alpha}+G^{*}\tilde{h}]=\tilde{p}^{\alpha}/\rho^{*}-\tilde{p}^{\beta}, \tag{34}$$

$$\sigma(\rho^{*}-1)\tilde{h}=\rho^{*}\tilde{w}^{\alpha}-\tilde{w}^{\beta}, \tag{35}$$

$$k^{*}\tilde{T}_{z}^{\alpha}-\tilde{T}_{z}^{\beta}=\rho^{*}\mathcal{L}_{\alpha\beta}(\tilde{w}^{\alpha}-\sigma\tilde{h}). \tag{36}$$

Equation (34) is the linearized version of the Clausius-Clapeyron equation for our system. Since we are working fairly close to the critical point, the densities of the two phases are comparable, and the pressures in each phase at the interface appear in this equation. In related work by Ozen and Narayanan,[19] an approximate version of the linearized Clausius-Clapeyron equation is employed that contains only the pressure in the vapor, valid in the limit $\rho^{*}\ll 1$. Our numerical results using their thermophysical properties are in fair agreement (within 10%), given the difference in the models.

E. Control parameter

Critical conditions are often determined experimentally by varying the temperature gradient across the system. The temperature gradient G_{β} appears in the dimensionless parameters Ma, Ra, $\mathcal{L}_{\alpha\beta}$, and $\mathcal{S}_{\alpha\beta}$. In order to study various combinations of the independent effects of buoyancy, latent heat, entropy, and the temperature dependence of the surface energy (Marangoni effect), it is convenient to introduce a separate dimensionless temperature gradient

$$\mathcal{G}=\frac{G_{\beta}d}{T_{E}}, \tag{37}$$

which can be used as a control parameter. We then introduce versions of the parameters Ma, Ra, $\mathcal{L}_{\alpha\beta}$, and $\mathcal{S}_{\alpha\beta}$ that are independent of G_{β} by setting

$$\mathrm{Ma}=\widetilde{\mathrm{Ma}}\,\mathcal{G},\quad \mathrm{Ra}=\widetilde{\mathrm{Ra}}\,\mathcal{G},\quad \mathcal{L}_{\alpha\beta}=\tilde{\mathcal{L}}_{\alpha\beta}/\mathcal{G},\quad \mathcal{S}_{\alpha\beta}=\tilde{\mathcal{S}}_{\alpha\beta}\mathcal{G}, \tag{38}$$

where

$$\widetilde{\mathrm{Ma}}=-\frac{\gamma_{T}T_{E}d}{\mu_{\beta}\kappa_{\beta}},\quad \widetilde{\mathrm{Ra}}=\frac{g\eta_{\beta}T_{E}d^{3}}{\nu_{\beta}\kappa_{\beta}},$$
$$\tilde{\mathcal{L}}_{\alpha\beta}=\frac{\rho_{\beta}L_{\alpha\beta}\kappa_{\beta}}{k_{\beta}T_{E}},\quad \tilde{\mathcal{S}}_{\alpha\beta}=\frac{s_{\alpha\beta}T_{E}d^{2}}{\nu_{\beta}\kappa_{\beta}}. \tag{39}$$

Linear stability calculations can then be performed by varying $\mathcal{G}$ for fixed values of $\widetilde{\mathrm{Ma}}$, $\widetilde{\mathrm{Ra}}$, $\tilde{\mathcal{L}}_{\alpha\beta}$, and $\tilde{\mathcal{S}}_{\alpha\beta}$; these parameters then can be set to zero to consider simplified systems.

III. NUMERICAL IMPLEMENTATION

We solve the eigenvalue problem that governs the linear stability of the system by using two complementary procedures. In the first approach, the equations are discretized using pseudospectral Chebyshev collocation, and the resulting generalized matrix eigenvalue problem is solved using the package RGG from the EISPACK software library.[33] For a discretization with N degrees of freedom, this routine produces approximations to the first N eigenvalues of the system; that is, values of the growth rate $\sigma=\sigma_{r}+i\sigma_{i}$ are obtained as a function of wavenumber for given values of the dimensionless input parameters given in Eqs. (18)–(21).

The second approach is to use the two-point boundary value solver BVSUP,[34] coupled with the root finder SNSQ,[35] both from the SLATEC library,[36] to implement a method described in Ref. 37 to solve the eigenvalue problem. In implementing this procedure, we generally set $\sigma_{r}=0$ and use the root finder to determine marginal values of σ_{i} and the control parameter $\mathcal{G}$ for each wavenumber. We then scan over wavenumbers to determine the critical conditions. The BVSUP procedure provides a very accurate solution for a given eigenmode provided a good enough initial estimate is available for the root-finding procedure.

The pseudospectral method is efficient for small values of N, and is well suited for searching parameter space to detect real and complex eigenvalues. Rather than performing fine grid calculations with the pseudospectral procedure, however, the coarse grid results from the pseudospectral method are often used as initial guesses for the BVSUP code. Continuation from previous solutions is also used once an eigenmode has been identified.

The BVSUP software works in a single domain, so we have mapped the two layers to a common domain by setting

$$\bar{z}=\begin{cases} z, & \text{for } 0<z<H_{\alpha}, \\ -H_{\alpha}z/H_{\beta}, & \text{for } -H_{\beta}<z<0, \end{cases} \tag{40}$$

so that $0<\bar{z}<H_{\alpha}$ in each phase. We then have

$$\frac{d}{dz}=\begin{cases} d/d\bar{z}, & \text{for } 0<z<H_{\alpha}, \\ (1/\ell)d/d\bar{z}, & \text{for } -H_{\beta}<z<0, \end{cases} \tag{41}$$

where $\ell=-H_{\beta}/H_{\alpha}$. To simplify the treatment of the problem, we also introduce an auxiliary ordinary differential equation in $\bar{z}$ for the interface $\tilde{h}$, by setting

$$\frac{d\tilde{h}}{d\bar{z}}=0, \tag{42}$$

which allows us to avoid eliminating $\tilde{h}$ as an unknown from the interface boundary conditions.

We generally present numerical results to five or more significant figures. This is done to facilitate comparison with other numerical calculations, although we note that material parameters are usually not known to this level of accuracy.

IV. RESULTS

In this section we present numerical results for the linear stability of the two-layer system, with thermophysical properties corresponding to the water-steam system.[38–40] The water-steam system has a critical point at temperature $T_{c}=647.096$ K, and we choose parameters at the lower temperature $T=640$ K, which is far enough below the critical point to allow an incompressible approximation for the flow field to be valid. Dimensional parameter values are given in Table I. Here, the surface energy is given by $\gamma=0.2358(1-\theta)^{1.256}[1-0.625(1-\theta)]$ J/m^{2}, where $\theta=T/T_{c}$.[38–40] Corresponding dimensionless parameters are given in Table II.

TABLE II. Dimensionless variables for the steam (α phase) water (β phase) system at T_E=640 K and p_E=202.7 bar.

Parameter	Symbol	Value
Ratio of densities	ρ^*	0.368
Ratio of dynamic viscosities	μ^*	0.506
Ratio of thermal conductivities	k^*	0.598
Ratio of thermal diffusivities	κ^*	0.819
Ratio of thermal expansion coefficients	η^*	1.86
Marangoni number	$\widetilde{\mathrm{Ma}}$	1.004×10^{8}
Rayleigh number	$\widetilde{\mathrm{Ra}}$	5.26×10^{8}
Dimensionless latent heat	$\tilde{\mathcal{L}}_{\alpha\beta}$	3.27×10^{-2}
Dimensionless entropy difference	$\tilde{\mathcal{S}}_{\alpha\beta}$	5.86×10^{14}
Crispation number	Cr	1.12×10^{-6}
Bond number	Bo	23.3
Prandtl number	Pr	3.50
Thickness parameter	ℓ	$-1/2$

In our calculations, we find that the stability of the system is quite sensitive to the parameters $\tilde{\mathcal{S}}_{\alpha\beta}$ and $\tilde{\mathcal{L}}_{\alpha\beta}$, and in fact the nature of the driving mechanism changes as the dimensionless entropy $\tilde{\mathcal{S}}_{\alpha\beta}$ varies from small to large values. The value of $\tilde{\mathcal{S}}_{\alpha\beta}$ for the water-steam system is quite large, and tends to mask the appearance of the Marangoni mode, as will be discussed below.

For the values of $\tilde{\mathcal{S}}_{\alpha\beta}$ that we consider for the water-steam system, we have not found any neutral modes for the case of heating from above, either with or without buoyancy. For the case of heating from below with buoyancy, the neutral curves shown in Fig. 2 are obtained. For this value of $\tilde{\mathcal{S}}_{\alpha\beta}$, we find that these modes are all insensitive to γ_T, in that setting $\widetilde{\mathrm{Ma}}=0$ does not affect the indicated modes. To emphasize the insensitivity to $\widetilde{\mathrm{Ma}}$, in Fig. 2 we plot results in terms of $\mathcal{G}$, as discussed in Sec. II E. Since we have

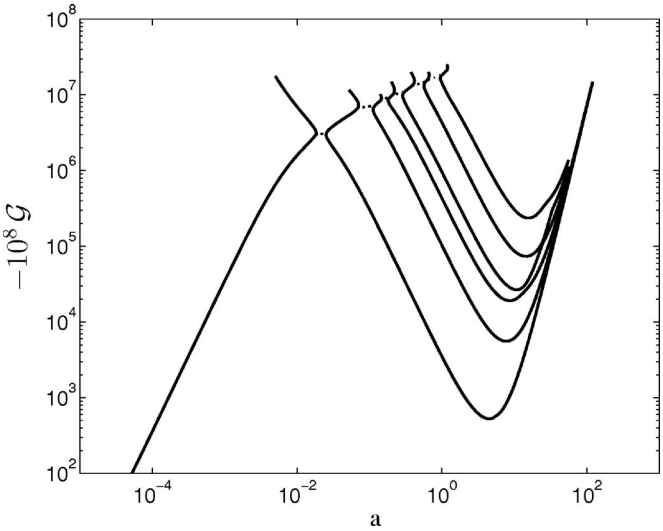

FIG. 2. Marginal stability curves for the water-steam system heated from below. Solid curves represent stationary modes, and the dotted curves represent oscillatory modes.

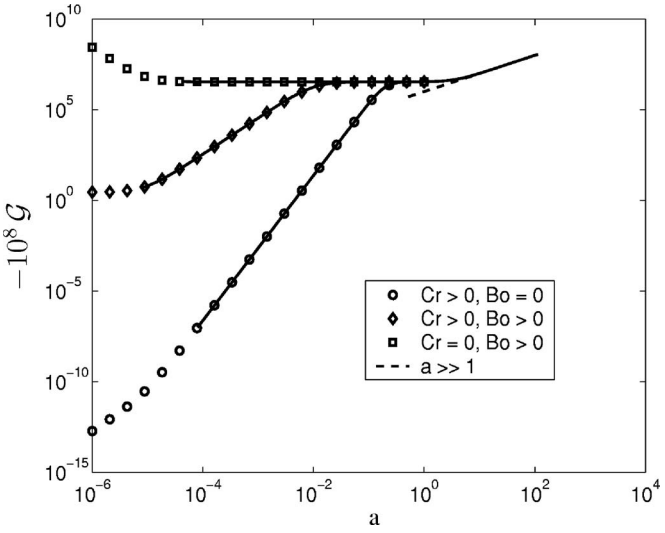

FIG. 3. Marginal stability curves for the water-steam system heated from below. Here, the effects of buoyancy are neglected by setting $\widetilde{\mathrm{Ra}}=0$. The solid curves represent numerical results, and the symbols correspond to a small wavenumber expansion. The dashed curve represents a large-wavenumber expansion.

$\mathrm{Ma}=\widetilde{\mathrm{Ma}}\,\mathcal{G}$ with $\widetilde{\mathrm{Ma}}\approx10^{8}$ for our choice of parameters, we plot the quantity $10^{8}\mathcal{G}$ to facilitate the comparison with Marangoni numbers. In Fig. 2, the most dangerous mode occurs at low wavenumbers, and is found to be insensitive to buoyancy as well. As mentioned in Sec. I, this is a novel two-phase mode that we discuss in more detail below. The remainder of the modes shown in Fig. 2 are all buoyant modes. There are oscillatory modes in Fig. 2 connecting regions where the low-wavenumber mode intersects the family of stationary buoyant modes; the oscillatory modes occur over very small ranges of wavenumber and are barely visible in the figure. The most dangerous of the buoyant modes has a critical wavenumber $a=4.5$ for $10^{8}\mathcal{G}=-527.19$, with unicellular flow mainly in the top layer and no significant interface deformation.

To better illustrate the mechanisms for instability, in this and in subsequent figures the displayed range of $\mathcal{G}$ values exceeds by several orders of magnitude the critical conditions. Although the linear stability model can be readily solved for large values of $\mathcal{G}$ (or Ra), the range of temperatures for which the linear model for the temperature dependence of the density as given in Eq. (5) is a reasonable approximation is generally much smaller than the extreme values given in the plots. However, the critical values of $\mathcal{G}$ are small enough that this approximation, and the more general Boussinesq approximations that we employ, are valid at the critical conditions. The rough criterion $|\rho-\bar{\rho}|/\bar{\rho}=\eta|T-T_R|/\bar{\rho}\ll1$ for the validity of Eq. (5) becomes, in dimensionless terms, $|\mathrm{Ra}|\ll\mathrm{Bo/Cr}$, and for our system, $\mathrm{Bo/Cr}=O(10^{7})$ and $\mathrm{Ra}=5.24\mathrm{Ma}$.

The low-wavenumber mode is shown in more detail in Fig. 3. In these calculations, we have eliminated the effects of buoyancy by setting $\widetilde{\mathrm{Ra}}=0$. To help understand this mode, we have also performed computations that illustrate the effects of the Bond number Bo and the Crispation number Cr

for this mode. Three cases are shown in Fig. 3; the case corresponding to Table II is the intermediate curve and symbols that asymptote to a small wavenumber limit for $10^8\mathcal{G}=-2.8$. The upper curve and symbols result from setting Cr=0, and the lower curve and symbols correspond to setting Bo=0. The solid curves correspond to numerical results, and the symbols on the curves correspond to analytical results from a small-wavenumber approximation given in the Appendix. The small-wavenumber results depend strongly on both Bo and Cr. For $\mathrm{Cr}\neq 0$ and $\mathrm{Bo}\neq 0$,

$$-10^8\mathcal{G}\approx\frac{d_1[1-\rho^*]\mathrm{Bo}}{d_2\mathrm{Cr}}=2.8351. \tag{43}$$

For Cr=0,

$$-10^8\mathcal{G}\approx\frac{-d_1}{d_4}a^{-2}-\frac{d_6}{d_4}=\frac{2.7668\times 10^6}{a^2}+3.4724\times 10^6. \tag{44}$$

For Bo=0 and $\mathrm{Cr}\neq 0$,

$$-10^8\mathcal{G}\approx\frac{d_1}{d_2\mathrm{Cr}}a^2=0.1925a^2. \tag{45}$$

The coefficients d_1, d_2, d_4, and d_6 depend on the layer geometry and the remaining material constants and are given in the Appendix; here we have evaluated these expressions for the values given in Table II. The curve for Cr>0 and Bo>0 reaches low values of $\mathcal{G}$ for small wavenumbers, corresponding to very shallow temperature gradients; in practice, a reasonable lower limit on the wavenumber that is set by a lateral container size would produce reasonable values for the critical temperature gradients. All three curves have the same behavior for larger wavenumbers, given by a large wavenumber approximation shown as the dashed curve. As described in the Appendix, this curve is given approximately by

$$-10^8\mathcal{G}\approx 1.0097\times 10^6 a. \tag{46}$$

For the parameter values in Table II, the low-wavenumber mode is insensitive to the Marangoni effect and, for low wavenumbers, to the effects of buoyancy. It is, however, quite sensitive to the entropy $\tilde{\mathcal{S}}_{\alpha\beta}$ and to the latent heat $\tilde{\mathcal{L}}_{\alpha\beta}$. To illustrate the sensitivity of the system to the parameters $\tilde{\mathcal{S}}_{\alpha\beta}$ and $\tilde{\mathcal{L}}_{\alpha\beta}$, we next consider calculations performed for various values of $\tilde{\mathcal{S}}_{\alpha\beta}$, while keeping the ratio of $\tilde{\mathcal{S}}_{\alpha\beta}$ and $\tilde{\mathcal{L}}_{\alpha\beta}$ fixed at its nominal value for the water-steam system under our chosen conditions.

In Fig. 4 we show neutral stability curves for the water-steam system heated from above (Ma>0) without buoyancy ($\widetilde{\mathrm{Ra}}=0$) for four values of $\tilde{\mathcal{S}}_{\alpha\beta}$. For $\tilde{\mathcal{S}}_{\alpha\beta}=0$, the system is unstable to a stationary mode with a critical wavenumber $a=2.7$ for Ma=227.20. The flow is mostly confined to the upper layer and is unicellular, without significant interface deformation. This neutral curve exhibits asymptotes at both smaller ($a=8.88\times 10^{-3}$) and larger ($a=7.76$) wavenumbers. As the entropy difference $\tilde{\mathcal{S}}_{\alpha\beta}$ increases, this mode is stabilized, and the wavenumbers of the asymptotes approach each other. For the largest value $\tilde{\mathcal{S}}_{\alpha\beta}=2.955\times 10^8$ shown in the figure, the range of unstable wavenumbers has contracted to $0.27<a<0.37$, and for slightly larger values of $\tilde{\mathcal{S}}_{\alpha\beta}$, the system is linearly stable. We note that the value of $\tilde{\mathcal{S}}_{\alpha\beta}$ for the water-steam system in Table II is $\tilde{\mathcal{S}}_{\alpha\beta}=5.86\times 10^{14}$, and for these parameter values (including the case $\widetilde{\mathrm{Ra}}\neq 0$) we have found no instabilities in heating from above.

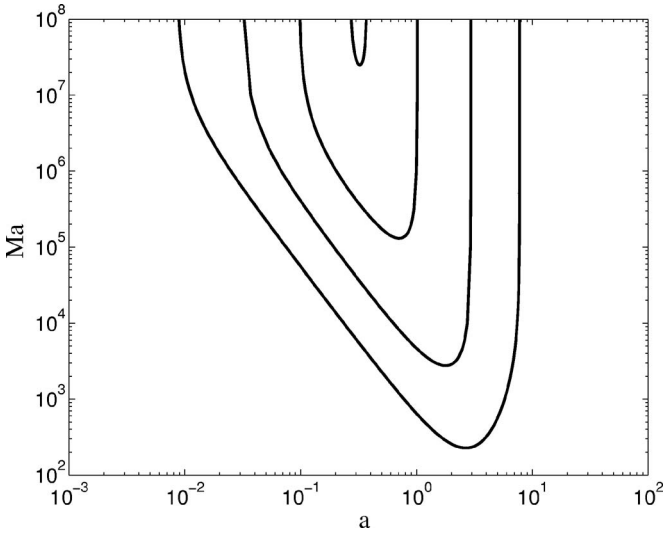

FIG. 4. Marginal stability curves for the water-steam system heated from above for various values of the entropy jump $\tilde{\mathcal{S}}_{\alpha\beta}$, keeping the ratio $\tilde{\mathcal{S}}_{\alpha\beta}/\tilde{\mathcal{L}}_{\alpha\beta}$ fixed. Here, the effects of buoyancy are neglected by setting $\widetilde{\mathrm{Ra}}=0$, and we have plotted $\mathrm{Ma}\approx 10^8\mathcal{G}$ vs the wavenumber a. From bottom to top, the curves correspond to $\tilde{\mathcal{S}}_{\alpha\beta}=0$, 2.5×10^8, 2.9×10^8, and 2.955×10^8, respectively.

In Fig. 5 we show neutral stability curves for the water-steam system heated from below (Ma<0) without buoyancy ($\widetilde{\mathrm{Ra}}=0$) for three values of $\tilde{\mathcal{S}}_{\alpha\beta}=0$, 2.955×10^8, and 3.5×10^8. For $\tilde{\mathcal{S}}_{\alpha\beta}=0$, the marginal stability curve has two stationary branches at high and low wavenumbers. The two branches have asymptotes for $a=8.88\times 10^{-3}$ and $a=7.76$, which are the same values obtained for the asymptotes of the marginal stability curve shown in Fig. 4 for $\tilde{\mathcal{S}}_{\alpha\beta}=0$ with heating from above (Ma>0). If the data are instead plotted as 1/Ma versus wavenumber, a single smooth neutral curve is obtained that passes through the points 1/Ma=0 at the wavenumbers corresponding to the asymptotes occurring in Figs. 4 and 5 for $\tilde{\mathcal{S}}_{\alpha\beta}=0$. For heating from below, there is a gap in wavenumber between the asymptotes where there is no stationary mode; instead, an oscillatory mode is observed that begins and ends with $\sigma_i=0$ at points on the stationary branches. The minimum on the $\tilde{\mathcal{S}}_{\alpha\beta}=0$ neutral curves occurs at a critical wavenumber $a=10.8$ for Ma=−4028.83. Similar behavior also occurs for $\tilde{\mathcal{S}}_{\alpha\beta}=2.955\times 10^8$, with a critical wavenumber $a=5.4$ for Ma=−681.22. In this case the distance between asymptotes of the stationary modes has decreased considerably, as in Fig. 4. For $\tilde{\mathcal{S}}_{\alpha\beta}=3.5\times 10^8$, the asymptotes have disappeared, and a single stationary mode occurs over the full range of wavenumbers. The minimum on

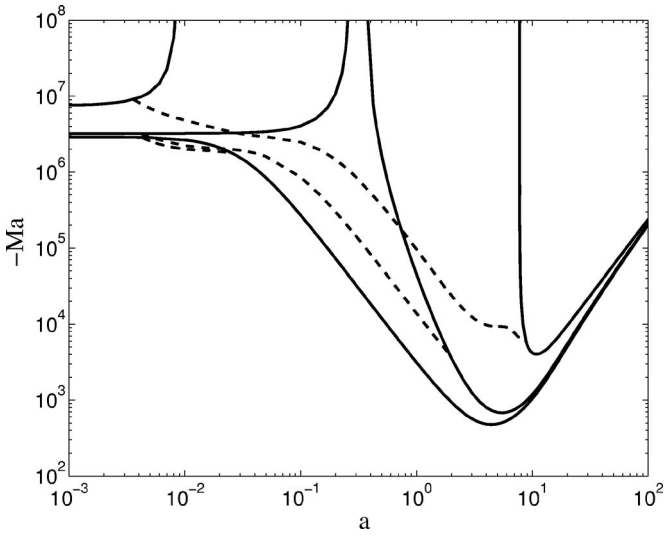

FIG. 5. Marginal stability curves for the water-steam system heated from below (Ma<0) for various values of the entropy jump $\tilde{\mathcal{S}}_{\alpha\beta}$, keeping the ratio $\tilde{\mathcal{S}}_{\alpha\beta}/\tilde{\mathcal{L}}_{\alpha\beta}$ fixed. Here, the effects of buoyancy are neglected by setting $\widetilde{\mathrm{Ra}}=0$. The solid curves represent stationary modes, and dashed curves correspond to oscillatory modes that connect to stationary modes with the same values of $\tilde{\mathcal{S}}_{\alpha\beta}$. From top to bottom on either the extreme left or extreme right sides of the plot, the stationary curves correspond to $\tilde{\mathcal{S}}_{\alpha\beta}=0$, 2.955×10^{8} and 3.5×10^{8}, respectively.

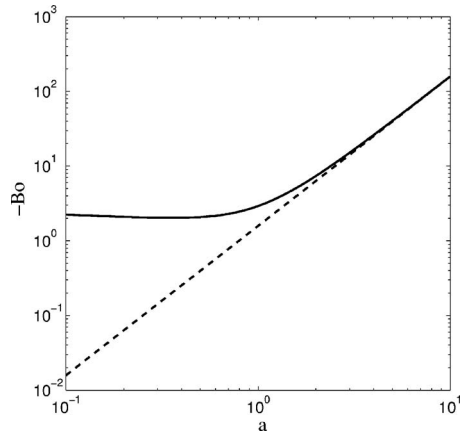

FIG. 6. Marginal stability curves for the water-steam system that is unstably stratified with respect to gravity. The dashed curve corresponds to the classical Rayleigh-Taylor instability in the absence of buoyancy, given by $-\mathrm{Bo}=a^2/(1-\rho^*)$. The solid curve represents numerical results that include the effects of buoyancy, with $\mathrm{Ma}=-1.0\times10^{6}$ and $\mathrm{Ra}=-5.24$ Ma.

the neutral curves occurs at a critical wavenumber $a=4.4$ for Ma$=-478.30$. Although there is no gap in wavenumber for the stationary mode in this case, an oscillatory mode persists over a small range of wavenumbers near $a=0.01$, as can be seen by careful examination of Fig. 5.

The low wavenumber mode in Fig 2 can be thus viewed as the continuation of the Marangoni mode shown in Fig. 5 for $\tilde{\mathcal{S}}_{\alpha\beta}=3.5\times10^{8}$ to much larger values of $\tilde{\mathcal{S}}_{\alpha\beta}$. In the process, the critical wavenumber has decreased significantly, and the Marangoni effect has been rendered ineffective by the large entropy. This can be seen from the boundary conditions given in Eqs. (33) and (34). For large values of $\tilde{\mathcal{S}}_{\alpha\beta}$, Eq. (34) shows that the interface becomes isothermal, and the Marangoni term in Eq. (33) that is proportional to the perturbed interface temperature is then negligible.

Rayleigh-Taylor instability

The two-layer system can also exhibit the classical Rayleigh-Taylor instability[10–14] if heavier fluid overlies lighter fluid. In the absence of buoyancy effects, the gravitational stability of the system is governed by a simple potential energy argument that balances the increased surface energy of a deformed interface $y=h(x)$ against the change in the gravitational potential energy of the displaced fluid,

$$g(\bar{\rho}_\alpha-\bar{\rho}_\beta)h=-\gamma h_{xx}. \tag{47}$$

In terms of our dimensionless variables, this takes the simple form

$$-\mathrm{Bo}=\frac{a^2}{(1-\rho^*)}, \tag{48}$$

which can be seen as a factor in the normal stress balance boundary condition (32).

In the situation we have studied above, we have lighter steam overlying heavier water, so the Rayleigh-Taylor instability does not occur. To study this instability for our system with a minimal change in notation, we temporarily choose to change the direction of gravity while keeping steam and water in the original orientation, so that the water and steam are unstably stratified with respect to gravity. We take $G_\beta<0$, so that buoyancy has a stabilizing effect on the system; the resulting sign conventions produce Ma<0, Ra>0, and Bo<0. Here we have modified the numerical procedure to compute marginal values of Bo as a function of wavenumber. In Fig. 6 we show the corresponding numerical results for the Rayleigh-Taylor instability. The dashed curve in Fig. 6 shows the curve $-\mathrm{Bo}=a^2/(1-\rho^*)$, which holds for $\widetilde{\mathrm{Ra}}=0$. The solid curve shows numerical marginal stability results for $\mathrm{Ma}=-1.0\times10^{6}$ and $\mathrm{Ra}=-5.24\mathrm{Ma}$. The stabilizing effects of buoyancy are evident at small wavenumbers, where the system is then stable if $|\mathrm{Bo}|$ is sufficiently small.

V. DISCUSSION

A mechanism for the two-phase instability can be identified in the large-wavenumber limit that is summarized in the Appendix. We ignore buoyancy by setting $\widetilde{\mathrm{Ra}}=0$, and also ignore interface deformation by setting Cr$=0$. To help visualize the flow, we introduce a two-dimensional streamfunction ψ with $w=\psi_x$ and $u=-\psi_z$.

The driving mechanism for the large-wavenumber instability arises from the coupling of the temperature field and vertical velocity that occurs in the thermal transport equations (25) and (29) and the latent heat boundary condition (36). The coupling is illustrated in the contours of the temperature and streamfunction, as shown in Fig. 7. To simplify the plot, we have assumed the material properties are equal

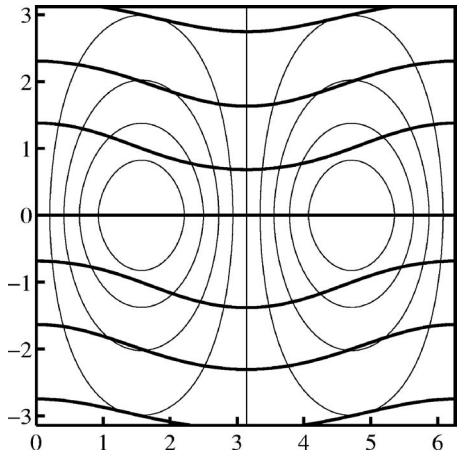

FIG. 7. Streamfunction contours (light lines) and temperature contours for the large-wavenumber solution with $a=1$ and equal material properties in both phases. The magnitude of the perturbation is exaggerated to emphasize the deformation of the temperature contours.

in both phases, and have exaggerated the size of the perturbation to emphasize the distortion of the isotherms near the interface. For the large value of $\mathcal{S}_{\alpha\beta}$ in the water-steam system, there is no significant interface deformation. The fluid flow is normal to the interface, and the plot shows that the downflow in the center of the plot tends to compress the distance between isotherms near the interface in the upper phase, and expand the distance between them in the lower phase. The opposite is true for the regions with upflow at the interface. The resulting net change in the temperature fluxes at the interface are balanced by the evolution of latent heat at the interface, which in turn is driven by the vertical velocity at the interface. When the system is heated from below as shown, these effects reinforce each other to drive the instability. When the system is heated from above, the effects are in opposing directions and no instability is possible.

The instability illustrated in Fig. 7 corresponds to the case of large entropy $\mathcal{S}_{\alpha\beta}$, and the Marangoni effect is negligible in this limit. For very small values of $\mathcal{S}_{\alpha\beta}$, the Marangoni effect becomes dominant and produces a large-wavenumber instability.

If the bilayer is heated from below, in the rest state the upper layer of gas is colder than the equilibrium temperature and the lower layer of liquid is hotter than the equilibrium temperature; these are both potentially destabilizing distributions. The pressure in the upper layer of gas is lower than the equilibrium pressure and the pressure in the lower layer of liquid is higher than the equilibrium pressure, which tends to stabilize the system. As discussed in Sec. I, a criterion for the underlying liquid (β phase) to be superheated is obtained by comparing the local pressure and temperature gradients at the interface with the Clausius-Clapeyron equation (1), giving

$$-G_\beta > \frac{g(\bar{\rho}_\beta/\bar{\rho}_\alpha - 1)}{(s_m^\alpha - s_m^\beta)}. \tag{49}$$

Similarly, the criterion for the overlying gas (α phase) to be supercooled is

$$-G_\alpha > \frac{g(1 - \bar{\rho}_\alpha/\bar{\rho}_\beta)}{(s_m^\alpha - s_m^\beta)}. \tag{50}$$

If we assume $\widetilde{\mathrm{Ra}}=0$ and $\widetilde{\mathrm{Ma}}=0$ in the small-wavenumber expansion given in the Appendix in Eq. (A1), we obtain the dimensional result

$$-G_\beta = \left[\frac{\rho^* d_1}{d_2^{(2)}}\right] \frac{g(\bar{\rho}_\beta/\bar{\rho}_\alpha - 1)}{(s_m^\alpha - s_m^\beta)}, \tag{51}$$

where the prefactor evaluates to $\rho^* d_1/d_2^{(2)}=0.465$ for our system. Thus, a supercooling argument is in qualitative agreement with the observed low-wavenumber instability. The supercooling argument is not expected to be quantitatively accurate, since it neglects the effects of capillarity and of flow, which arise when there are lateral pressure and temperature gradients in the system.

VI. CONCLUSIONS

We have performed linear stability calculations for horizontal fluid bilayers that can undergo a phase transformation, taking into account both buoyancy effects and thermocapillary effects. We mainly consider the case of the lighter phase overlying the heavier phase, so that the base state is stably stratified in this sense. We find that the two-phase system can be linearly unstable to heating either from above ($\mathrm{Ma}>0$) or below ($\mathrm{Ma}<0$). More specifically, for small values of the entropy difference $\widetilde{\mathcal{S}}_{\alpha\beta}$ between the phases, the marginal stability curve, if plotted as $1/\mathrm{Ma}$ versus the wavenumber a, is smooth with both positive and negative values (see Figs. 4 and 5). The zeroes of this curve then represent wavenumbers for which a plot of Ma versus wavenumber exhibits vertical asymptotes. The two-phase instability persists to small wavenumbers in the case of heating from below. For the larger values of $\widetilde{\mathcal{S}}_{\alpha\beta}$ that characterize the water-steam system, we find that the two-phase system is unstable only for heating from below (see Fig. 2). The large value of $\widetilde{\mathcal{S}}_{\alpha\beta}$ renders the system insensitive to the value of γ_T for heating both from above and below in the water-steam system, and the Marangoni effect is masked by a stronger effect due to the morphological instability driven by the large entropy difference across the interface. The absence of a Marangoni effect for the two-phase system was previously noted by Ozen and Narayanan.[19] From our calculations, the basic reason for the absence of the Marangoni effect in the water-steam system is that, because of the large magnitude of dp/dT, typical values of the pressure variation are insufficient to cause appreciable deviations of the interface from isothermality; hence, there is no driving force for the Marangoni instability. We have confirmed numerically that if the entropy difference is artificially reduced to values significantly lower than that for the water-steam system, the Marangoni instability does become active.

To help understand the mechanisms driving the instability on heating from below, we have performed both long-wavelength and short-wavelength analyses of the two-phase system. The short-wavelength analysis (large a) shows that the instability is driven by a coupling between the flow normal to the interface and the latent heat generation at the

interface (see Fig. 7). For the large-wavelength (small a) instability (see Fig. 3), the exponent n in the leading order expansion $\mathrm{Ma} \sim a^n$ depends on the Crispation and Bond numbers as well as on $\tilde{\mathcal{S}}_{\alpha\beta}$. We also note that the two-phase system allows a conventional Rayleigh-Taylor instability if the heavier fluid overlies the lighter fluid;[10–14] applying a temperature gradient allows a stabilization of the interface (see Fig. 6).

ACKNOWLEDGMENTS

G.B.M. and S.R.C. were supported by the Microgravity Research Division of NASA, and K.F.G and D.L.C. were supported by National Research Council Postdoctoral Fellowships during a portion of this research. The authors are grateful for helpful discussions with D. M. Anderson, J. B. Andrews, N. Martys, and B. T. Murray.

APPENDIX: LARGE AND SMALL WAVENUMBER EXPANSIONS

Here we consider the limits of large and small wavenumbers. We introduce the dimensionless layer widths $\bar{H}_\alpha = H_\alpha/d = 1/(1-\ell)$ and $\bar{H}_\beta = H_\beta/d = -\ell/(1-\ell)$, where $d = H_\alpha + H_\beta$ and $\ell = -H_\beta/H_\alpha = -1/2$ in our calculations.

A. Small wavenumbers

Small-wavenumber asymptotics can be performed in the two-phase case for general values of Ra. Since there are several possible cases to consider for the two-phase system depending on the assumed values of Ma, Ra, $\mathcal{L}_{\alpha\beta}$, and $\mathcal{S}_{\alpha\beta}$, we use the dimensionless temperature gradient $\mathcal{G}$ as a control parameter, so that the dimensionless parameters $\widetilde{\mathrm{Ma}}$, $\widetilde{\mathrm{Ra}}$, $\tilde{\mathcal{L}}_{\alpha\beta}$, and $\tilde{\mathcal{S}}_{\alpha\beta}$ can all appear as independent quantities in the expansion coefficients. For $\mathrm{Bo} \neq 0$ and $\mathrm{Cr} \neq 0$, we find the leading order result

$$\mathcal{G} = \frac{d_1\,\mathrm{Bo}(\rho^* - 1)}{\mathrm{Cr}(d_2 + d_5\,\widetilde{\mathrm{Ra}})}, \tag{A1}$$

where

$$d_1 = \frac{4}{3\rho^*}[\bar{H}_\alpha + k^*\bar{H}_\beta]\{4\bar{H}_\alpha\bar{H}_\beta\mu^*[\bar{H}_\beta^2 + (\rho^*)^2\bar{H}_\alpha^2] + 6\bar{H}_\alpha^2\bar{H}_\beta^2\mu^*\rho^* + [\bar{H}_\beta^4(\mu^*)^2 + \bar{H}_\alpha^4(\rho^*)^2]\}, \tag{A2}$$

$$d_2 = d_2^{(1)}\,\widetilde{\mathrm{Ma}} + d_2^{(2)}\tilde{\mathcal{S}}_{\alpha\beta}, \tag{A3}$$

$$d_2^{(1)} = \frac{8}{\rho^*}\bar{H}_\alpha\bar{H}_\beta\mu^*[1-\rho^*][\bar{H}_\beta + \rho^*\bar{H}_\alpha], \tag{A4}$$

$$d_2^{(2)} = \frac{4}{3}(3\bar{H}_\alpha^2\bar{H}_\beta^2\mu^*[1+\rho^*] + 4\bar{H}_\alpha\bar{H}_\beta\mu^* \times [\bar{H}_\beta^2 + \rho^*\bar{H}_\alpha^2] + [\bar{H}_\alpha^4\rho^* + \bar{H}_\beta^4(\mu^*)^2]), \tag{A5}$$

$$d_5 = \frac{(1-k^*)(1-\rho^*)}{15k^*\rho^*}\{23\mu^*\bar{H}_a\bar{H}_b[k^*\bar{H}_b^4 + \eta^*(\rho^*)^2\bar{H}_a^4] + 7[k^*(\mu^*)^2\bar{H}_b^6 + \eta^*(\rho^*)^2\bar{H}_a^6] + 15\mu^*\rho^*\bar{H}_a^2\bar{H}_b^2[k^*\bar{H}_b^2 + \eta^*\bar{H}_a^2]\}. \tag{A6}$$

For the values given in Table II, we have

$$d_1 = 0.508\,715, \quad d_2 = 2.365\,61 \times 10^{14}, \quad d_5 = 0.032\,388, \tag{A7}$$

$$d_2^{(1)} = 0.893\,976, \quad d_2^{(2)} = 0.402\,588. \tag{A8}$$

$\widetilde{\mathrm{Ra}} = 0$

For the case with $\widetilde{\mathrm{Ra}} = 0$, the dispersion relation for $\sigma = 0$ can again be evaluated symbolically in closed form. The result can then be expanded for small wavenumbers, giving

$$0 = a^8\{d_1[\rho^* - 1]\mathrm{Bo} - d_2\mathrm{Cr}\mathcal{G}\} + a^{10}\{-\mathcal{G}(d_3\mathrm{Cr} + d_4 \times [\rho^* - 1]\mathrm{Bo}) - (d_1 - d_6[\rho^* - 1]\mathrm{Bo})\} + O(a^{12}). \tag{A9}$$

The expression can be solved for $\mathcal{G}$ as a rational expression of the form

$$\mathcal{G} = \frac{d_1[\rho^* - 1]\mathrm{Bo} - (d_1 - d_6[\rho^* - 1]\mathrm{Bo})a^2}{d_2\mathrm{Cr} + (d_3\mathrm{Cr} + d_4[\rho^* - 1]\mathrm{Bo})a^2} + O(a^4). \tag{A10}$$

The coefficients d_1 and d_2 are as given above, and d_3, d_4, and d_6 are given by

$$d_3 = \widetilde{\mathrm{Ma}}\,d_3^{(1)} + \tilde{\mathcal{S}}_{\alpha\beta}d_3^{(2)}, \tag{A11}$$

$$d_4 = \widetilde{\mathrm{Ma}}\,d_4^{(1)} + \tilde{\mathcal{S}}_{\alpha\beta}d_4^{(2)}, \tag{A12}$$

$$d_6 = d_6^{(1)} + \widetilde{\mathrm{Ma}}\,\tilde{\mathcal{L}}_{\alpha\beta}d_6^{(2)} + \tilde{\mathcal{L}}_{\alpha\beta}\tilde{\mathcal{S}}_{\alpha\beta}d_6^{(3)}, \tag{A13}$$

with

$$d_3^{(1)} = \frac{4}{3\rho^*}\bar{H}_\alpha\bar{H}_\beta \times (3\bar{H}_\alpha\bar{H}_\beta\mu^*[\bar{H}_\alpha - (\rho^*)^2\bar{H}_\beta] + 2\bar{H}_\alpha\bar{H}_\beta\mu^*[\bar{H}_\beta - (\rho^*)^2\bar{H}_\alpha] + \mu^*[\bar{H}_\beta^3 - (\rho^*)^2\bar{H}_\alpha^3] + 2[(\mu^*)^2\bar{H}_\beta^3 - (\rho^*)^2\bar{H}_\alpha^3] + 3\mu^*\rho^*[\bar{H}_\alpha^3 - \bar{H}_\beta^3] + \bar{H}_\alpha\bar{H}_\beta\mu^*\rho^*[\bar{H}_\beta - \bar{H}_\alpha]), \tag{A14}$$

$$d_3^{(2)} = \frac{2}{45}(15\bar{H}_\alpha^2\bar{H}_\beta^2\mu^*[\bar{H}_\alpha^2 + \rho^*\bar{H}_\beta^2] + 90\bar{H}_\alpha^3\bar{H}_\beta^3\mu^*[1+\rho^*] + 55\bar{H}_\alpha^2\bar{H}_\beta^2\mu^*[\bar{H}_\beta^2 + \rho^*\bar{H}_\alpha^2] + 44\bar{H}_\alpha\bar{H}_\beta\mu^*[\bar{H}_\beta^4 + \rho^*\bar{H}_\alpha^4] + 65\bar{H}_\alpha^2\bar{H}_\beta^2[(\mu^*)^2\bar{H}_\beta^2 + \rho^*\bar{H}_\alpha^2] + 10\bar{H}_\alpha\bar{H}_\beta[(\mu^*)^2\bar{H}_\beta^4 + \rho^*\bar{H}_\alpha^4] + 9[(\mu^*)^2\bar{H}_\beta^6 + \rho^*\bar{H}_\alpha^6]), \tag{A15}$$

$$d_4^{(1)} = \frac{-1}{30\rho^*\kappa^*}\bar{H}_\alpha^2\bar{H}_\beta^2 \times \{5\bar{H}_\alpha^2\bar{H}_\beta^2[\bar{H}_\beta\mu^* - \bar{H}_\alpha(\rho^*)^2\kappa^*] - 7\bar{H}_\alpha\bar{H}_\beta\rho^*[\bar{H}_\alpha^3 - \bar{H}_\beta^3\mu^*\kappa^*] - 2[\bar{H}_\alpha^5(\rho^*)^2 - \bar{H}_\beta^5\mu^*\kappa^*]\}, \tag{A16}$$

$$d_4^{(2)} = \frac{-1}{90\kappa^*}\bar{H}_\alpha^3\bar{H}_\beta^3 \times (14\bar{H}_\alpha\bar{H}_\beta[\bar{H}_\alpha^2 + \bar{H}_\beta^2\mu^*\rho^*\kappa^*] + 11\bar{H}_\alpha^2\bar{H}_\beta^2[\mu^* + \rho^*\kappa^*] + 3[\bar{H}_\alpha^4\rho^* + \bar{H}_\beta^4\mu^*\kappa^*]), \tag{A17}$$

$$d_6^{(1)} = \frac{2}{45\rho^*}(60\mu^*\bar{H}_\alpha^3\bar{H}_\beta^3[\bar{H}_\alpha + k^*(\rho^*)^2\bar{H}_\beta] + 84\mu^*\bar{H}_\alpha^2\bar{H}_\beta^2[\bar{H}_\beta^3 + k^*(\rho^*)^2\bar{H}_\alpha^3] + 100\mu^*\bar{H}_\alpha^3\bar{H}_\beta^3[k^*\bar{H}_\beta + (\rho^*)^2\bar{H}_\alpha] + 44\mu^*\bar{H}_\alpha\bar{H}_\beta[k^*\bar{H}_\beta^5 + (\rho^*)^2\bar{H}_\alpha^5] + 35\bar{H}_\alpha^3\bar{H}_\beta^3[(\mu^*)^2\bar{H}_\beta + k^*(\rho^*)^2\bar{H}_\alpha] + 19\bar{H}_\alpha\bar{H}_\beta[(\mu^*)^2\bar{H}_\beta^5 + k^*(\rho^*)^2\bar{H}_\alpha^5] + 45\bar{H}_\alpha^2\bar{H}_\beta^2[k^*(\mu^*)^2\bar{H}_\beta^3 + (\rho^*)^2\bar{H}_\alpha^3] + 9[k^*(\mu^*)^2\bar{H}_\beta^7 + (\rho^*)^2\bar{H}_\alpha^7] + 60\mu^*\rho^*\bar{H}_\alpha^2\bar{H}_\beta^2[\bar{H}_\alpha^3 + k^*\bar{H}_\beta^3] + 120\mu^*\rho^*\bar{H}_\alpha^3\bar{H}_\beta^3[\bar{H}_\beta + k^*\bar{H}_\alpha]), \tag{A18}$$

$$d_6^{(2)} = \tfrac{2}{3}\bar{H}_\alpha^3\bar{H}_\beta^3[\mu^*\bar{H}_\beta^2 - \rho^*\bar{H}_\alpha^2], \tag{A19}$$

$$d_6^{(3)} = \tfrac{4}{9}\bar{H}_\alpha^4\bar{H}_\beta^4\rho^*[\bar{H}_\alpha + \mu^*\bar{H}_\beta]. \tag{A20}$$

For the values given in Table II, the additional constants are given by

$$d_3 = 7.171\,45 \times 10^{13}, \quad d_4 = -1.84596 \times 10^{11}, \quad d_6 = 6.3844 \times 10^9. \tag{A21}$$

Essentially the same values for d_j are obtained by setting $\tilde{\mathrm{Ma}}=0$; thus, the small-wavenumber behavior of the system is insensitive to the Marangoni effect for the parameters in Table II.

B. Large wavenumbers

We next consider the limit of large wavenumbers for a stationary mode. For our system, the numerical results suggest that buoyancy effects and interface deformation are unimportant in this limit, so we also consider the formal limit of small Crispation number, i.e., $\mathrm{Cr}\to 0$, along with $\mathrm{Ra}=0$. For $\mathrm{Ra}=0$, the governing equations for the velocity field are decoupled from the thermal field, which simplifies the analysis. For $\mathrm{Cr}\to 0$, the dimensionless form of the normal momentum balance,

$$\mathrm{Cr}(\tilde{p}^\alpha - \tilde{p}^\beta) - \mathrm{Bo}(\rho^* - 1)\tilde{h} + a^2\tilde{h} = 2\mathrm{Cr}(\mu^*\tilde{w}_z^\alpha - \tilde{w}_z^\beta), \tag{A22}$$

then reduces to

$$\mathrm{Bo}(\rho^* - 1)\tilde{h} - a^2\tilde{h} = 0. \tag{A23}$$

For $\mathrm{Bo}(\rho^*-1)-a^2 \neq 0$, we conclude that the interface deformation vanishes; i.e., $\tilde{h}=0$.

In the limit of large wavenumber, the disturbances are concentrated near the interface and the effects of the outer boundaries are insignificant. The appropriate solution can then be computed using decay conditions in an unbounded domain as $z \to \pm\infty$. The vertical components of the velocity field are given by

$$\tilde{w}^\alpha(z) = A_\alpha e^{-az} + B_\alpha a z e^{-az}, \quad \tilde{w}^\beta(z) = A_\beta e^{az} + B_\beta a z e^{az}. \tag{A24}$$

The temperature fields are given by

$$\tilde{T}^\alpha(z) = \frac{-G^*A_\alpha}{2a^2\kappa^*}[az]e^{-az} - \frac{G^*B_\alpha}{4a^2\kappa^*}[az]e^{-az} - \frac{G^*B_\alpha}{4a^2\kappa^*}[a^2z^2]e^{-az} + C_\alpha e^{-az}, \tag{A25}$$

$$\tilde{T}^\beta(z) = \frac{A_\beta}{2a^2}[az]e^{az} - \frac{B_\beta}{4a^2}[az]e^{az} + \frac{B_\beta}{4a^2}[a^2z^2]e^{az} + C_\beta e^{az}. \tag{A26}$$

The corresponding horizontal velocities and pressures are

$$\tilde{u}^\alpha = i(B_\alpha - A_\alpha)e^{-az} - iB_\alpha a z e^{-az}, \quad \tilde{u}^\beta = i(B_\beta + A_\beta)e^{az} + iB_\beta a z e^{az}, \tag{A27}$$

and

$$\tilde{p}^\alpha = 2\rho^*\nu^* a B_\alpha e^{-az}, \quad \tilde{p}^\beta = 2aB_\beta e^{az}. \tag{A28}$$

The interface boundary conditions determine the remaining six constants A_α, B_α, C_α, A_β, B_β, and C_β, leading to the relations

$$A_\beta = \rho^* A_\alpha, \quad B_\beta = B_\alpha - (1+\rho^*)A_\alpha, \quad C_\beta = C_\alpha, \tag{A29}$$

and

$$A_\alpha = \frac{\mathrm{Ma}\,\mathcal{S}_{\alpha\beta}(1-\kappa^*) + 8a^3\kappa^*(\nu^*-1)(1+k^*)}{\Delta}C_\alpha, \tag{A30}$$

$$B_\alpha = \frac{\mathrm{Ma}\,\mathcal{S}_{\alpha\beta}R - 8a^3\kappa^*(1+\rho^*)(1+k^*)}{\Delta}C_\alpha, \tag{A31}$$

where

$$\Delta = 2a[(1+\rho^*)(1-\kappa^*) + R(\nu^*-1)], \tag{A32}$$

$$R = -[\kappa^*(1+3\rho^*) + 2 + 4a\kappa^*\rho^*\mathcal{L}_{\alpha\beta}/\mathrm{Ma}]. \tag{A33}$$

The dispersion relation takes the form

$$\left\{\frac{\Delta_1}{2(1+\mu^*)} - \mathcal{S}_{\alpha\beta}(1-\kappa^*-R_1)\right\} \times \mathrm{Ma} = 8a^3\kappa^*(1+k^*)[(\nu^*+\rho^*)] - \mathcal{S}_{\alpha\beta}R_2 - \frac{\Delta_2}{2(1+\mu^*)}, \tag{A34}$$

where

$$R_1 = -[\kappa^*(1+3\rho^*) + 2], \quad R_2 = -4a\kappa^*\rho^*\mathcal{L}_{\alpha\beta}, \tag{A35}$$

$$\Delta_1 = 2a[(1+\rho^*)(1-\kappa^*) + R_1(\nu^*-1)], \quad \Delta_2 = 2aR_2(\nu^*-1). \tag{A36}$$

For interpreting the large-wavenumber two-phase mode, we consider the limit of large entropy $\mathcal{S}_{\alpha\beta}$, which produces some simplification by eliminating the Marangoni effect and making the interface isothermal with $\tilde{T}^\alpha = \tilde{T}^\beta = 0$. We then have $C_\alpha = C_\beta = 0$, $A_\beta = \rho^* A_\alpha$, $B_\alpha = A_\alpha$, and $B_\beta = -\rho^* A_\alpha$. We note that the steady-state vertical velocity fields and temperature fields then take the form

$$\tilde{w}^\alpha(x,z) = A_\alpha[1+(az)]e^{-az}\cos az, \quad \tilde{w}^\beta(x,z) = \rho^* A_\alpha[1-(az)]e^{az}\cos az, \tag{A37}$$

$$\tilde{T}^\alpha(x,z) = G^* z - \frac{(az)G^*}{4a^2\kappa^*}[3+(az)]A_\alpha e^{-az}\cos az, \tag{A38}$$

$$\tilde{T}^\beta(x,z) = z + \frac{(az)\rho^*}{4a^2}[3-(az)]A_\alpha e^{az}\cos az. \tag{A39}$$

The resulting dispersion relation then has the simple form

$$\frac{\mathrm{Ma}}{\mathcal{L}_{\alpha\beta}} = \frac{k_\beta G_\beta}{\rho_\beta L_{\alpha\beta}(\kappa_\beta/d)} = -\frac{4\kappa^*\rho^*}{3(1+\kappa^*\rho^*)}a. \tag{A40}$$

[1] R. W. Zeren and W. C. Reynolds, "Thermal instabilities in two-fluid horizontal layers," J. Fluid Mech. **53**, 305 (1972).
[2] E. N. Ferm and D. J. Wollkind, "Onset of Rayleigh-Bénard-Marangoni instability, Comparison between theory and experiment," J. Non-Equilib. Thermodyn. **7**, 169 (1982).
[3] S. H. Davis, "Thermocapillary instabilities," Annu. Rev. Fluid Mech. **19**, 403 (1987).
[4] D. D. Joseph and Y. Y. Renardy, *Fundamentals of Two-Fluid Dynamics* (Springer-Verlag, Berlin, 1993).
[5] D. Johnson and R. Narayanan, "Marangoni convection in multiple bounded fluid layers and its application to materials processing," Philos. Trans. R. Soc. London, Ser. A **356**, 885 (1998).
[6] C. D. Andereck, P. W. Colovas, M. M. Degen, and Y. Y. Renardy, "Instabilities in two-layer Rayleigh-Bénard convection, overview and outlook," Int. J. Eng. Sci. **36**, 1451 (1998).
[7] M. F. Schatz and G. P. Neitzel, "Experiments on thermocapillary instabilities," Annu. Rev. Fluid Mech. **33**, 93 (2001).
[8] A. A. Nepomnyashchy, M. G. Verlarde, and P. Colinet, *Interfacial Phenomena and Convection* (Chapman & Hall/CRC, London, 2002).
[9] J. S. Turner, *Buoyancy Effects in Fluids* (Cambridge University Press, Cambridge, UK, 1973).
[10] D. Y. Hsieh, "Effects of heat and mass transfer on the Rayleigh-Taylor instability," J. Basic Eng. **94**, 156 (1972).
[11] D. Y. Hsieh, "Interfacial stability with mass and heat transfer," Phys. Fluids **21**, 745 (1978).
[12] S-P. Ho, "Linear Rayleigh-Taylor stability of viscous fluids with mass and heat transfer," J. Fluid Mech. **101**, 111 (1980).
[13] X. Chen and E. Fried, "Rayleigh-Taylor problem for a liquid-liquid phase interface," J. Fluid Mech. **560**, 395 (2006).
[14] O. Ozen and R. Narayanan, "A note on the Rayleigh-Taylor instability with phase change," Phys. Fluids **18**, 042110 (2006).
[15] F. H. Busse and G. Schubert, "Convection in a fluid with two phases," J. Fluid Mech. **46**, 801 (1971).
[16] F. H. Busse, "Fundamentals of thermal convection," in *Mantle Convection, Plate Tectonics and Global Dynamics*, edited by W. R. Peltier (Gordon & Breach, New York, 1989), pp. 23–95.
[17] S. Sakurai, A. Tschammer, W. Pesch, and G. Ahlers, "Convection in the presence of a first-order phase change," Phys. Rev. E **60**, 539 (1999).
[18] J. Margerit, P. Colinet, G. Lebon, C. S. Iorio, and J. C. Legros, "Interfacial nonequilibrium and Bénard-Marangoni instability of a liquid-vapor system," Phys. Rev. E **68**, 041601 (2003).
[19] O. Ozen and R. Narayanan, "The physics of evaporation and convective instabilities in bilayer systems, linear theory," Phys. Fluids **16**, 4644 (2004).
[20] A. Huang and D. D. Joseph, "Instability of the equilibrium of a liquid below its vapour between horizontal heated plates," J. Fluid Mech. **242**, 235 (1992).
[21] C. A. Ward and D. Stanga, "Interfacial conditions during evaporation or condensation of water," Phys. Rev. E **64**, 051509 (2001).
[22] D. M. Anderson, P. Cermelli, E. Fried, M. E. Gurtin, and G. B. McFadden, "General dynamical sharp-interface conditions for phase tranformations in viscous heat-conducting fluids," J. Fluid Mech. **581**, 323 (2007).
[23] D. M. Anderson, G. B. McFadden, and A. A. Wheeler, "A phase-field model with convection, sharp-interface asymptotics," Physica D **151**, 305 (2001).
[24] D. A. Edwards, H. Brenner, and D. T. Wasan, *Interfacial Transport Processes and Rheology* (Butterworth-Heinemann, Boston, 1991).
[25] D. M. Anderson, G. B. McFadden, and A. A. Wheeler, "Diffuse-interface methods in fluid mechanics," Annu. Rev. Fluid Mech. **30**, 139 (1998).
[26] D. M. Anderson, G. B. McFadden, and A. A. Wheeler, "A phase-field model of solidification with convection," Physica D **135**, 175 (2000).
[27] J. S. Langer, "Instabilities and pattern formation in crystal growth," Rev. Mod. Phys. **52**, 1 (1980).
[28] W. A. Tiller, K. A. Jackson, J. W. Rutter, and B. Chalmers, "The redistribution of solute atoms during the solidification of metals," Acta Metall. **1**, 428 (1953).
[29] W. W. Mullins and R. F. Sekerka, "Morphological instability of a particle growing by diffusion or heat flow," J. Appl. Phys. **34**, 323 (1963).
[30] W. W. Mullins and R. F. Sekerka, "Stability of a planar interface during solidification of a dilute binary alloy," J. Appl. Phys. **35**, 444 (1964).
[31] S. H. Davis, *Theory of Solidification* (Cambridge University Press, Cambridge, UK, 2001).
[32] H. B. Callen, *Thermodynamics* (John Wiley & Sons, New York, 1960).
[33] B. T. Smith, J. M. Boyle, J. J. Dongarra, B. S. Garbow, Y. Ikebe, V. C. Klema, and C. B. Moler, *Matrix Eigenvalue Routines -EISPACK Guide* (Springer-Verlag, Berlin, 1976).
[34] M. R. Scott and H. A. Watts, "Computational solution of linear two-point boundary-value problems via othonormalization," SIAM (Soc. Ind. Appl. Math.) J. Numer. Anal. **14**, 40 (1977).
[35] M. J. D. Powell, "A hybrid method for nonlinear equations," in *Numerical Methods for Nonlinear Algebraic Equations*, edited by P. Rabinowitz (Gordon & Breach, New York, 1970), pp. 87–114.
[36] W. H. Vandevender and K. H. Haskell, "The SLATEC mathematical subroutine library," SIGNUM Newsl. **17**, 16 (1982); As of September 2007,

the SLATEC library is available at http://www.netlib.org/slatec. The program SNSQ was written by K. Hiebert and is based on an algorithm of Powell (Ref. 35).
[37]H. B. Keller, *Numerical Solution of Two-Point Boundary Value Problems* (Society for Industrial and Applied Mathematics, Philadephia, 1976), pp. 45–48.
[38]W. Wagner, *Properties of Water and Steam* (Springer-Verlag, Berlin, 1998).
[39]A spreadsheet for the thermodynamical properties of water and steam has been developed by Bernhard Spang, BUCO Waermeaustauscher GmbH, Sandstr-31, Geesthacht, Schleswig-Holstein, Germany. As of September 2007, the spreadsheet is available at http://www.cheresources.com/iapwsif97.shtml
[40]W. T. Parry, J. C. Bellows, J. S. Galligher, and A. H. Harvey, *ASME International Steam Tables for Industrial Use* (ASME Press, New York, 2000).